Exploring constituent redistribution in irradiated U-19Pu-14Zr fuel via electron probe microanalysis

Wright, Karen E.; Lecrivain, Lindsey; Pincock, Cortney; Coleman, Magen; Wiscaver, Pamela; Barker, Beau; Gimenes Rodrigues Albuquerque, Luiza; Capriotti, Luca; Aitkaliyeva, Assel

DOI
10.1016/j.jnucmat.2024.155411

Publication date
2025

Document Version
Final published version

Published in
Journal of Nuclear Materials

Journal of Nuclear Materials 603 (2025) 155411

Contents lists available at ScienceDirect

Journal of Nuclear Materials

journal homepage: www.elsevier.com/locate/jnucmat

Exploring constituent redistribution in irradiated U-19Pu-14Zr fuel via electron probe microanalysis

Karen E. Wright [a,b,*], Lindsey Lecrivain [a], Cortney Pincock [a], Magen Coleman [a], Pamela Wiscaver [a], Beau Barker [a], Luiza Gimenes Rodrigues Albuquerque [a], Luca Capriotti [a], Assel Aitkaliyeva [c]

[a] Idaho National Laboratory, PO Box 6000, Idaho Falls, ID 83415, USA
[b] Department of Radiation Science and Technology, Faculty of Applied Sciences, Delft University of Technology, Delft, the Netherlands
[c] Materials Science and Engineering, University of Florida, PO Box 116400, Gainesville, FL 32611, USA

HIGHLIGHTS

- EPMA and Q-ICP-MS analyses of U, Pu, and Zr in irradiated metallic fuel are within 3% of each other.
- EPMA analyses show that four compositionally distinct fuel zones exist comprising U, Pu, and Zr.
- Pu content across the pin diameter varies from a low of approximately 8 wt.% to a high of 22 wt. %.
- EPMA can quantify U, Pu, and Zr atoms lost or gained from each compositional zone.

ARTICLE INFO

Keywords:
U-Pu-Zr fuel
Constituent redistribution
Electron probe microanalysis
Irradiated

ABSTRACT

The phenomena of constituent redistribution, wherein a previously homogeneous metallic fuel forms discrete, radially concentric compositional zones upon irradiation was investigated by examining an irradiated U-19Pu-14Zr fuel (where numbers represent wt. %) with a burnup of 11.5 at.% with electron probe microanalysis (EPMA) and quadruple inductively coupled plasma mass spectroscopy (Q-ICP-MS).

EPMA-generated U, Pu, and Zr compositional data obtained from a diameter traverse of the sample was converted to mass and was used to: 1) compare the overall fuel element analysis results between the two methods, 2) determine the number of compositionally distinct zones forming as a result of constituent redistribution; and 3) quantify the post-irradiation loss or gain of U, Pu, and Zr atoms in each distinct compositional zone.

Weight percent concentrations of U, Pu, and Zr for the overall cross section compare favorably between the two analytical methods, suggesting that the spatially resolved EPMA analysis complements bulk chemical analysis.

Among the four identified compositional zones, post-irradiation quantification of U, Pu, and Zr elemental atom content changes shows that the quantity of U atoms lost from the innermost zone is slightly less than the quantity of U atoms gained by the middle two zones, and the quantity of Zr atoms lost from the high-U third zone is slightly less than is gained by the two innermost zones. Pu is lost from all four zones, although the innermost zone and the high-U third zone lose a significantly higher percentage (> 22 %) of their initial Pu atoms than the other two zones. For all three elements, EPMA cannot distinguish between atoms lost due to transport to a different zone from atoms lost due to nuclear processes; however, the insight gained from using this process can be used to experiment with new modeling techniques to predict constituent redistribution in U-Pu-Zr fuels.

* Corresponding author at: Idaho National Laboratory, PO Box 1625, MS 6000, Idaho Falls, ID 83415, USA.
E-mail address: Karen.Wright@inl.gov (K.E. Wright).

https://doi.org/10.1016/j.jnucmat.2024.155411
Received 30 May 2024; Received in revised form 20 August 2024; Accepted 16 September 2024
Available online 17 September 2024

1. Introduction

1.1. Metallic fuels and fast reactors

Generation-IV nuclear reactors, including the sodium fast reactor (SFR), are a part of a low-carbon energy generation strategy intended to help mitigate the deleterious effects of climate change. Advantages of the SFR include the reactor's ability to act as a burner that can be used to transmute minor actinides thus reducing waste, or a converter (a breeder reactor that has a near 1:1 ratio between fissile material consumed and fissile material produced), or a breeder reactor in which excess fissile material is produced [1].

Sodium fast reactors using metallic fuels have been in use since the 1950's, including the reactors EBR-I and EBR-II in Idaho, and the FERMI-I and Dounreay Fast Reactor in the UK [2]. Reasons for the selection of metallic fuel include relative ease of fabrication, high thermal conductivity, and high fissile and fertile density [3]. In addition, pyroprocessing spent metallic fuel provides the opportunity to recycle fuel in a proliferation resistant manner [4], thus decreasing security concerns and facilitating resource reclamation.

Because of these advantages, metallic fuels irradiated in fast neutron spectrum reactors have been studied for several decades. One notable behavioral phenomenon—constituent redistribution, was reported by Murphy et al. in 1969 [5]. Constituent redistribution occurs in the fuel during irradiation, rendering a previously homogeneous alloy inhomogeneous. Depending on whether the Zr content increases or decreases in the fuel center, potentially deleterious effects can occur such as phase transformations, decreasing solidus temperatures, and local changes in fissile density, which can negatively impact the physical and mechanical properties of the fuel, leading to fuel performance problems [6].

Since this behavior was initially reported, numerous experimental investigations [6–9], and modeling efforts [10–16] have been devoted to studying and predicting this aspect of irradiated metallic fuel behavior. Porter et al. [7] provides a good description of the constituent distribution phenomenon. The following is a summary of their findings along with some more recent observations:

- Constituent redistribution occurs in U-Pu-Zr alloys containing more than 8 wt.% Pu as well as U-Zr alloys lacking Pu [11].
- Constituent redistribution in U-Pu-Zr alloys begins as early as 1.9 at. % burnup and becomes more pronounced with increasing burnup.
- Fuel swelling and bubble growth occur early in the irradiation process and precede elemental redistribution.
- When moving along a radius from the pin's center to the pin's periphery, several phase-field boundaries are crossed, each of which has different Zr solubility. Zr solubility is controlled by temperature gradients found in the pin; thus, a diffusion driving force is created by heat flow and the chemical potential of the elements in these phases [7,11]. A schematic of the three phase fields identified by composition in a part of the pin subject to burnup of at least 1.9 at.% and sampled from x/L > 0.5 is shown below (Fig. 1), where L=1 represents the pin's full length and x represents the sample location as a fraction of the full pin length as measured from the bottom to top of the pin. At x/L > 0.5 the pin temperature is generally hotter than at x/L < 0.5, and it is in this hotter region in which the model described by Fig. 1 applies.
- The presumed γ phase, which is high in Zr, occurs in the center. For a U-Pu-Zr alloy containing 15 at. % Pu, this phase begins to stabilize with a Zr content of approximately 45 at% at 640°C.
- At the same temperature and Pu composition, the presumed γ + ζ phase field, located near mid-radius, begins to stabilize with a Zr content of approximately 3 at.%. This zone is thought to result from Zr migration from that phase field toward the center and the periphery, while U migrates from the center toward mid-radius and the cladding.
- The outer-most phase region, comprising presumed δ and ζ phases, is compositionally similar to the as-fabricated composition, with Zr concentrations increasing toward the cladding.
- Pu is either immobile or its concentration changes are insignificant [6,9,10,12–15].

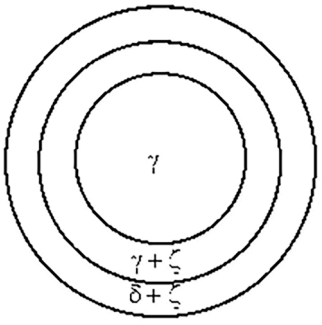

Fig. 1. Shows the phase-field boundaries observed following irradiation in high-power locations within the pin [7]. See text for details.

1.2. Historical electron microprobe use on irradiated metallic fuels

Because the gas flow through proportional detectors and other electronics can be radiologically shielded, and because the electron beam interaction volume in metallic nuclear fuel is relatively small (~1 μm ^{3}, as modeled using Casino v. 2.51 [17]), electron probe microanalysis (EPMA) has been used for many decades for quantitative irradiated nuclear fuel analysis. Early examples of EPMA-based metallic fuel analysis include Argonne National Laboratory's (ANL's) late 1980's to early 1990's era constituent redistribution studies [18–21] while the METAPHIX studies performed by the Joint Research Center and the Central Research Institute of Electric Power Industry [22,23] represent recent high-quality work.

The difficulty of using ANL's legacy metallic fuel EPMA data [18–21] in modern applications is several-fold: 1) standards were not employed consistently; 2) none of the reports available to authors of the present study reported using peak overlap corrections. This presents a problem for U-Pu-Zr fuels as the U Mβ X-ray line significantly overlaps the Pu Mα X-ray line, meaning that measuring the Pu concentration in the presence of a significant U concentration without overlap correction will produce over-estimates of the Pu concentration; 3) Ref. [20] states specifically that no matrix correction algorithms were employed, while Refs. [19,21] make no reference to matrix correction algorithms; 4) not many points were acquired and those that were used a large, defocused beam (~40 μm diameter) to collect an "average analysis" of that region, the result of which is that some significant elemental concentration changes may not have been detected; and 5) few publicly available reports of EPMA analysis of irradiated U-Pu-Zr fuels exist from that era, and that limited set of data has been used to construct constituent redistribution models.

This study focuses on the EPMA analysis of irradiated 67U-19Pu-14Zr (where the preceding numbers indicate weight percent) fuel with the following objectives:

1. Measure radial element concentrations across the diameter using modern EPMA methods that include the use of appropriate standards, peak overlap corrections, and matrix correction algorithms.
2. Use collected compositional data to define distinct compositional zones that formed as the result of constituent redistribution.
3. Describe the general characteristics of each zone.
4. Use this data to quantify fuel element gain or loss from each compositional zone.

2. Experimental

2.1. Fuel fabrication and irradiation

Fuel for the X441 portion of the Design Parameter-1 experiment was fabricated and cast as described by [24]. This was a one-step process that combined alloy preparation and injection casting together in an argon atmosphere glovebox. Alloying materials were first rendered homogenous and were then injection-cast into ZrO_2-coated quartz molds. Following casting, slugs were removed from molds, cut to size, loaded into jackets containing sodium, and then heated in a settling furnace. Fabricated slugs were clad in D9 austenitic stainless steel with a 75% smear density prior to irradiation. Compositional and available isotopic data for the as-fabricated alloy are shown in Table 1.

The fuel was irradiated in fast reactor EBR-II, with salient end-of-irradiation parameters shown in Table 2.

Additional data concerning this experiment and engineering scale post irradiation examination results are available from Capriotti et al. [25].

2.2. Sample preparation

The two fuel rod samples examined in this study were cut from the x/L = 0.65 location of the rod, which is above the rod's peak power location at x/L~0.5. The first radial cross section for EPMA analysis was mounted in a metallography mount and fixed in place with epoxy. It was then polished with diamond suspensions and water to a 0.5 μm final finish and coated with 15 nm of Al to increase sample conductivity during EPMA analysis. The second radial cross section was dissolved and examined using quadrupole inductively coupled plasma mass spectroscopy (Q-ICP-MS) to determine the chemical and isotopic composition of the material (see Section 2.4).

2.3. EPMA analysis

Electron probe microanalysis was performed using a Cameca SX100R EPMA shielded to 3 Ci of ^{137}Cs. Method details are available in Wright et al. [26] and are comparable to those employed by Ritter et al. [27]. In summary, quantitative analyses were conducted with a 25 keV accelerating voltage and beam currents ranging from 40-200 nA depending on the type of analysis. The beam was focused, and the step size employed in diameter traverses ranged from 10-50 μm with attempts made to avoid porosity. Probe for EPMA v. 13.3.1 [28] was used to collect and process quantitative point data while Cameca Peak Sight (v. 5.1) [29] and Probe Image (1.3.5.2115) [30] were used for map acquisition. All X-ray data was corrected for peak overlaps using Probe for EPMA (for points) and CalcImage v. 13.3.1 [28] for X-ray maps. Following overlap correction, absorbance, fluorescence, and atomic number corrections were performed with the PAP [31] matrix correction algorithm. Transuranic element mass absorption coefficients (MACs) came from the Farthing and Walker database [32] while MACs for lower Z elements came from Heinrich MAC30. Oxygen MACs came from the Pouchou and Pichoir database [33].

Table 1
Alloy weight percent composition with isotope (as available).

Isotope	wt% of alloy
U-234	0.57
U-235	54.92
U-236	0.25
U-238	11.26
Pu-239	16.71
Pu-240	2.09
Pu-241	0.16
Pu-242	0.04
Zr*	14.0

* isotopic content was not available

Table 2
End-of-irradiation data for fuel element A814 from the X441A experiment.

Composition	Burnup (at%)	Inner Clad Temperature (°C) *	Linear Power Average (kW/m)	Linear Power Peak (kW/m)
U-19Pu-14Zr	11.53	588.69	45.3	50.6

* measured at the top of the fuel column

Fig. 2 shows a backscattered electron image (BSE) of the pin cross section illustrating the analyzed areas. X-ray maps of the diameter are enclosed by the large vertical black box (box 1) and are shown in Fig. 3a. Boxes 2-4 enclose X-ray mapped regions shown in Figs. 4, 6, and 7, respectively. Findings from these analyses are detailed in Section 3. Results from a quantitative vertical traverse extending through the fuel from N to S are shown in Fig. 3b. Because U, Pu, and Zr azimuthal symmetry was assumed, one diameter traverse was used in this work. Note that N, S, E, and W refer to directional annotations on Fig. 2 and do not relate to rod orientation in the reactor.

2.4. Bulk analysis

2.4.1. Dissolution summary

The sample intended for Q-ICP-MS was received into the analytical laboratory as a solid small, flat, dark, gray-colored cylinder. After initial observation, it was placed in a tared Erlenmeyer flask and weighed. An analytical blank was prepared alongside the sample to account for any changes to the sample due to the analytical process. To the sample and blank, 25 mL of plasma grade water (Ultra-Trace Fisher Scientific Water)

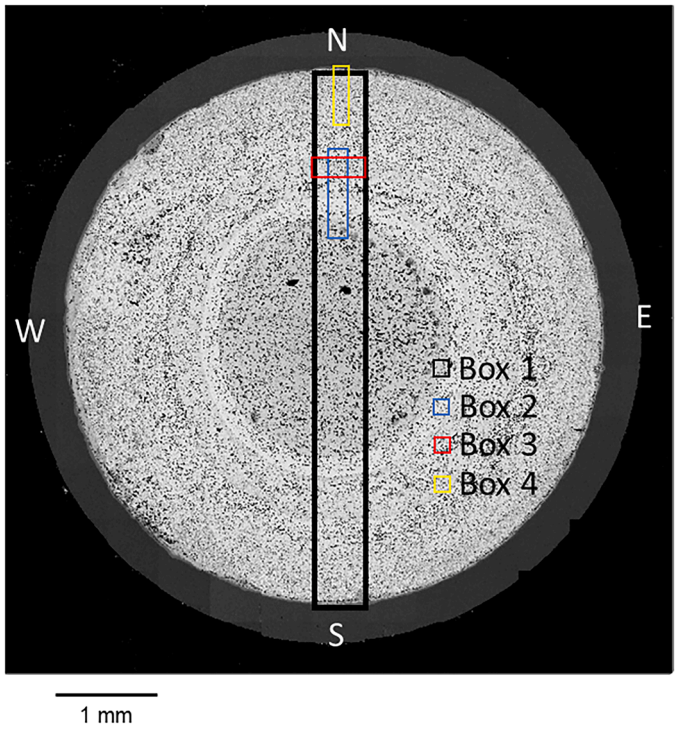

Fig. 2. Shows a backscatter electron image of the pin cross section with the pin diameter X-ray map region indicated by the long, vertical box 1. Additional "box" locations shown are referenced elsewhere in this work. Quantitative compositional point data was obtained from the N-S diameter extending vertically through the fuel from N to S. For descriptive ease the image has been annotated with compass directions, but these directions do not relate to the rod's orientation in the reactor.

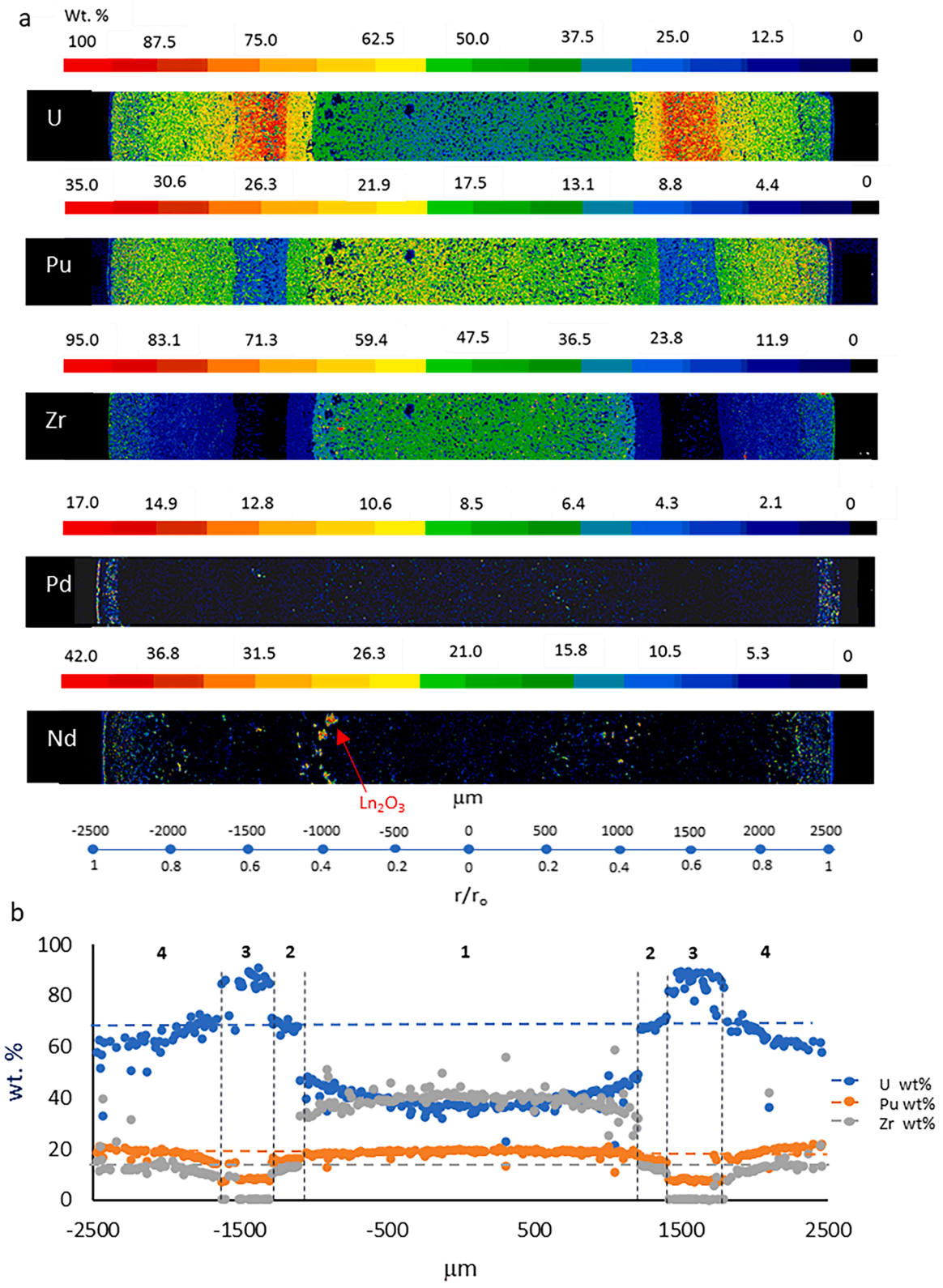

Fig. 3. (a, b). a) shows quantitative X-ray maps (U, Pu, Zr, Pd, Nd) of the region shown in Fig. 2a Box 1; b) shows a quantitative elemental vertical traverse measured down the center of Box 1 (Fig. 2a). Distinct compositional zones 1-4 are separated by vertical dotted lines. The pre-irradiation composition of each fuel element is indicated by horizontal lines corresponding to the colors shown in the legend. Both diagrams are oriented with the N side to the left. 99% CI error bars are smaller than the symbols.

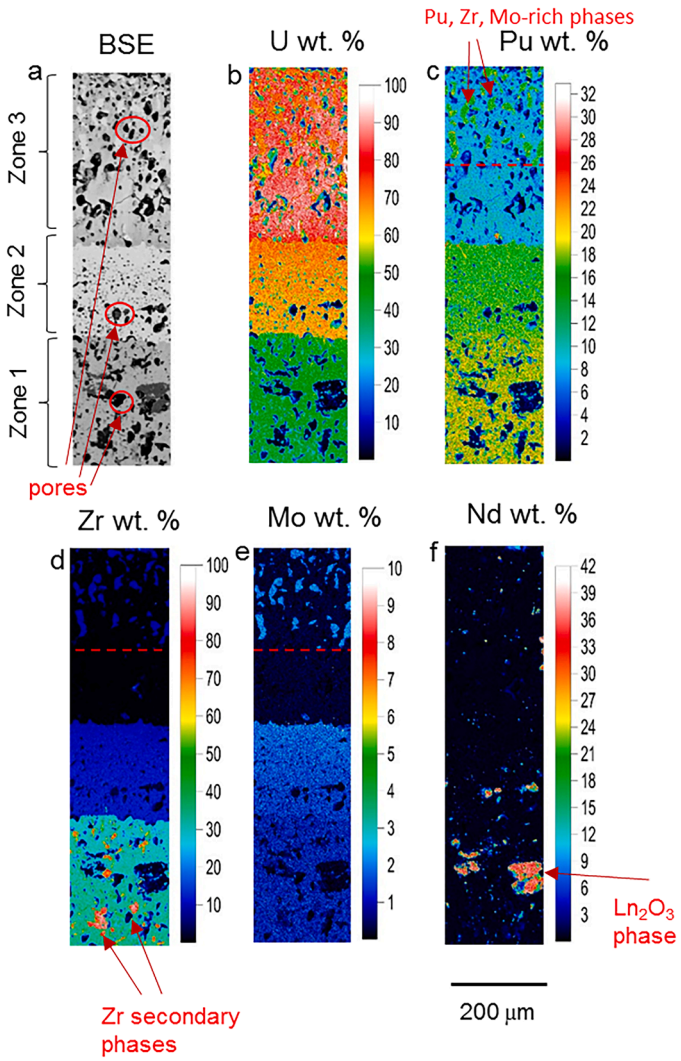

Fig. 4. (a–f) a) BSE micrograph of the transition between Zone 1 and Zone 3. Quantitative weight percent X-ray maps of the transition shown in b-f for b) U; c) Pu; d) Zr; e) Mo; and f) Nd. The red dotted line shown in c-e delineates the portion of Zone 3 that contains secondary phases from the portion of Zone 3 where they are absent. The X-ray map and BSE image location is shown in Fig. 2, Box 2.

was added, with no noted reactions. A mixture containing 25 mL of 12 M HCl (Fisher Scientific Optima Grade HCl) and 0.25 mL of 24 M HF (Fisher Scientific Optima Grade HF) was added slowly, and a reaction was observed (the sample turned opaque black) until approximately 5 mL of the mixture were added. Once 25 mL of HCl/HF was added, the sample and blank were left to react at ambient temperature overnight. Flasks were then placed on a hot plate set to 177°C and reduced in volume to approximately 25 mL. To the sample and blank, 25 mL of 16 M HNO_3 (Optima grade Fisher Scientific Nitric Acid) was then added, changing the solution color from a dark blue-green to brown. The sample and blank were returned to hot plate set to 177°C and heated until the blank was colorless. After that, 2.5 mL of 4% boric acid was added to the sample and blank and then heated at 204°C until reduced in volume to approximately 25 mL. Once cooled, the sample and blank were transferred to tared bottles and diluted to 50 mL with 2 M HNO_3, and then the final solution weight was recorded.

2.4.2. Quadrupole inductively coupled plasma mass spectroscopy

The sample was analyzed for isotopic quantities of fission products and actinides using an Elan DRC2 Q-ICP-MS instrument. All dilutions were made on a weight-to-weight basis using calibrated analytical balances in a 5% nitric acid solution (Optima grade Fisher Scientific Nitric Acid and Ultra-Trace Fisher Scientific Water). Dilution concentrations were based on the initial sample weight and elements or isotopes being measured.

Calibration of the instrument was performed daily, and calibration standards were run prior to analysis of the samples. The Zr analytical standard for the Q-ICP-MS calibration was prepared from a stock solution (High Purity Standards 10 µg g^{-1}) [34] and diluted to prepare working calibration standards with concentrations between 0 to 5 ng g^{-1}. The calibration standards were made in a 5% nitric acid solution (Optima grade Fisher Scientific Nitric Acid and Ultra-Trace Fisher Scientific Water) to ensure that the matrix of the calibration standards matched that of the samples. Uranium and Plutonium were calibrated by using dilutions of certified reference material standards produced by New Brunswick Laboratory [35,36]; concentrations of the dilutions were confirmed by Multicollector-ICP-MS measurements before use in Q-ICP-MS. Four internal standards (Sc, In, Ho and Bi) were used in the analysis to account for plasma fluctuations throughout the analysis and were prepared by the same method as the calibration standards.

After the measurements for a given group of analytes was completed, a secondary (check) standard with a known concentration of the analytes was measured to confirm that the calibrations were constant over the course of a run. The secondary standards were prepared in the same way as the calibration standards and were independent from the standards used to calibrate the instrument. For the fission products, stock solutions of the secondary standards were obtained from Inorganic Ventures. For uranium, a natural uranium standard manufactured by High Purity Standards was used [34].

The signal for each isotope was measured three times from which the average value and relative standard deviations were calculated. The uncertainty in the Q-ICP-MS measurements was estimated using statistical software (GUM Workbench© Pro version 2.4.1.406) [37]. All reported uncertainties were 95% confidence interval values. Secondary standards were also compared to known values to ensure the instrument and analysis was calibrated correctly for each isotope.

3. Results

3.1. Overall observations

X-ray maps of U, Pu, Zr, Pd, and Nd are shown in Fig. 3a; Fig. 3b shows results from quantitative traverse point analysis down the vertical diameter (Fig. 2). Compositional zone designations overlay traverse data that are separated by vertical dotted lines. Horizontal dotted lines illustrate the pre-irradiation concentration for each fuel element (Fig. 3b). Unlike the three-zone model discussed in Section 1.1 and shown in [12] for an axial location of x/L= 0.67 (similar to x/L = 0.65 for this work), these data show four distinct compositional zones. The magnitude of the U, Pu, and Zr compositional changes occurring within each zone is evident.

Fig. 3a appears to show that fuel elements U and Zr retain azimuthal symmetry following irradiation but Pu shows some asymmetry, For example, the Pu concentration on Zone 1's north side is slightly higher than on its south side, and the Pu concentration at the Zone 4 fuel cladding interface is slightly higher than the same interface on the north side; however, these differences are relatively small (< 5%, relative).

The post-irradiation U concentration in the pin center (Zone 1) is approximately 37 wt. %, which is almost one-half of its pre-irradiation concentration (i.e, 67 wt. %). In Zone 3, the post-irradiation U attains concentrations as high as ~ 90 wt. %, which is approximately 35% greater than its pre-irradiation value. Zr compositional changes are contrary to U concentration variations. Pu composition varies across the pin from a low of approximately 8 wt. % in Zone 3 to a high of 22 wt. % near the cladding in Zone 4, while the Pu concentration in Zone 1 and Zone 2 averages approximately 18 wt.% and 15 wt. %, respectively.

With a factor of approximately three between the lowest and highest observed Pu concentrations, this work shows a significantly larger Pu compositional range than reported in previous works [6,9–15].

Among fission products, rare earth element precipitates, some of which are in oxide form, are distributed radially near the Zone 1 periphery. As measured by EPMA, Am, Y, and lanthanide (Ln) elements, concentrated as precipitates toward the periphery of Zone 1's outer rim (Fig. 3a), were found to have a stoichiometry of approximately Ln_2O_3 (Table 3). Stoichiometry determinations were based on EPMA oxygen and Ln, Am, and Y measurements and presume that elements Am, Y, and Ln exist in the 3+ oxidation state. Fuel and fission product elements were also detected in these phases, although detection of these elements can also result from secondary fluorescence.

The oxygen source for this phase is not clear. Since water was used in the polishing process, it is possible that Ln, Am, and Y were oxidized during polishing. Lanthanides and Pd are concentrated in the fuel-cladding interfacial zone on the N and S sides of the pin (Fig. 3a).

Fig. 4 (a–f) shows an enhanced view of a portion of the compositional changes that occur between Zone 1 and Zone 3. Fig. 4a shows that while large elongate pores are present in Zone 1 and Zone 3, pores in Zone 2 tend to be smaller and rounder. Pores in Zone 1 are commonly filled with lanthanide elements (Fig. 4f). Note that these Ln-rich precipitates do not occur with Pd (as they do closer to the cladding), but rather with O in an Ln_2O_3 stoichiometry, as determined by EPMA measurements. Pores in Zone 3 tend to lack lanthanide element accumulations (Fig. 4f).

Compositionally the zones are distinct, with abrupt transitions between them. Secondary Zr phases, which are stabilized by O, C, and N contaminants present during pin fabrication [38], can be seen in Zone 1 (Fig. 4d) but were not observed to extend into Zones 2 or 3. Two phases comprising Zone 3 can be seen in Fig. 4 (c–e). The less abundant of the two is enriched in Pu, Zr, and Mo, while the surrounding matrix phase is higher in U, lower in Pu and contains relatively little Zr and Mo compared to the former phase.

When considering U, Pu, and Zr only, the overall average element concentration in Zone 4 is similar to the fabrication composition. However, the concentration of each of those elements changes substantially between the Z3-Z4 interface and the cladding (Fig. 3b). In addition, lanthanide elements accumulate near the cladding—some associated with Pd (Fig. 3a) while some appear to occur as oxides. Additionally, Pu and Zr increase toward the cladding while the U concentration decreases (Fig. 3b).

ImageJ v. 1.51k [39] was used to measure porosity in each of the four compositional zones. A BSE image was obtained from each zone present in the northern radius (north portion of the black box in Fig. 2). The area represented by each image is shown in Table 3. Each image was binarized followed by manual threshold adjustment before porosity was calculated. Results are shown in Table 4. As a result of Zone 2 being thinner than the other zones, the Zone 2 analyzed area was much smaller than the area analyzed for the remaining zones.

Table 3
Shows the composition of the presumed Ln_2O_3 phase.

Element	wt%	at%
Mo	<0.07	
Ru	<0.1	
Rh	<0.07	
Pd	<0.06	
U	0.59	0.17
Pu	0.50	0.14
Am	0.08	0.02
Ce	6.80	3.37
Nd	36.4	17.4
La	4.30	2.13
Pr	7.50	3.67
Eu	0.23	0.10
Gd	0.46	0.20
Sm	11.0	5.05
Ba	0.17	0.09
Zr	2.48	1.90
Y	10.6	8.23
O	13.4	57.6
sum	94.5	

3.2. Zone detail

3.2.1. Zones 1 and 2

Fig. 5 shows a BSE micrograph of the pin center. At approximately 2300 μm in diameter, Zone 1 is relatively wider than what has been observed in the more commonly studied U-19Pu-10Zr systems, as this zone is thought to enlarge with increasing Zr content [40]. The center is characterized by numerous pores, many of which have elongated as two or more pores have merged (Fig. 5).

Morphologically Zone 2 has smaller pores than are observed in Zone 1 and it differs chemically from Zone 1 (Fig. 3b). Fig. 3b shows the U concentration increases from approximately 37 wt.% to 67 wt.% between Zone 1 and Zone 2 while the Zr concentration falls from approximately 37 wt.% to 11 wt. %. At approximately 200 μm thick, Zone 2 is substantially narrower than the other zones and its intra-zonal composition changes significantly. Between its interfaces with Zone 1 and Zone 3, U increases by approximately 7 % (relative) while Zr decreases by 25% (relative).

3.2.2. Zone 3

As viewed in Fig. 2, Zone 3 varies in thickness from approximately 300 μm along the west side of the sample to approximately 390 μm on the south side of the sample. Zone 3 is composed of two distinct phases; one phase is rich in Pu, Zr, and Mo, exhibits low porosity, and tends to be elongated in shape with the long axis oriented approximately parallel to the radial direction (Fig. 6d, bright phase). It comprises approximately 25% of the mass in the Zone 3 region. The second phase is U-rich and Zr-poor and comprises the remaining 75% of the non-porous mass. The composition of both phases is shown in Table 5. Although the analytical total (Table 5) for the high Zr phase is close to 100%, the analytical total for the high U phase is approximately 95%, which is lower than expected for EPMA analysis. The reason for this low total is uncertain. In addition to the elements listed in Table 5, elements such as La, Pr, Eu, Gd, Sm, Xe, I, Rh, and Pd were measured; however, concentrations of those elements were below the method detection limit. Wavelength scans through the available Rowland circle range were collected using Quartz, LiF, PET, and TAP crystals; however, no significant missing elements were observed.

3.2.3. Zone 4

Zone 4 thickness ranges from approximately 800-900 μm. Fig. 7 (a–h) shows the outer 480 μm portion of Zone 4 as it is seen on the north side of the pin (Fig. 3a).

Zone 4 is characterized by the presence of several different phases, as shown by the varying gray-scale levels in Fig. 7a and corresponding X-ray map images (Fig. 7b–h). At the bottom of Fig. 7b (closer to the pin center) U-rich phases are much more abundant than other phases but decrease in abundance beginning approximately 200 μm before the cladding is encountered (toward the top of Fig. 7b). Concomitant with this uranium concentration decrease, Pu and Zr concentrations increase. Approximately 10-20 μm before the cladding is contacted, U and Pu

Table 4
Shows percent porosity for each compositional zone as measured by ImageJ v. 1.51k [39] and the area used for the porosity analysis.

Zone	Porosity %	Area Dimension (μm ^{2})
1	32	250000
2	18	36000
3	19	204000
4	32	164800

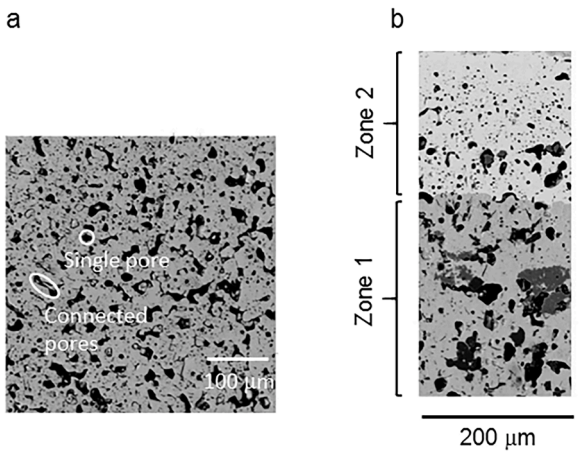

Fig. 5. (a, b). a) BSE micrograph of Zone 1 at the pin center; b) BSE micrograph showing the porosity difference between Zones 1 and 2.

concentrations decrease while Zr increases. Increased Zr in the fuel region in immediate contact with the cladding is the result of the fuel casting process wherein Zr precipitates out of the melt that is in contact with the quartz mold and forms a rind around the fuel periphery (Figs. 3b and 7 (b–d)).

The most notable change observed in this region occurs with Ln element behavior. Although Ln elements are present throughout this region (Fig. 7e), further from the cladding they appear as elemental lanthanide phases or in some instances they appear to be oxides (possibly a result of water use while polishing); however, approximately 200 µm from the cladding, the Ln elements in solid solution combine into phases with Pd and Rh (Fig. 7 e–h), which can occur via the peritectic reaction (Eq. (1)) [41]:

$$Nd_{(ss)} + Pd_{(s)} = Nd_7Pd_3\ (T < 690\ ^\circ C) \quad (1)$$

Discussion

4.1. EPMA-based quantification compared to ICP-MS

EPMA is a quantitative elemental analysis technique that makes it possible to use collected data to estimate fuel element mass changes between identified zones. To quantify mass movement across the pin, each compositional point measured along the radial traverse (Fig. 3b) represents a semicircular slice whose radius increases with distance from the pin center. Each slice's width is equal to the distance between two consecutive measured points, with a thickness equivalent to the beam interaction volume of about 1 μm^3. The weight percent elemental composition of the elements comprising each slice is converted to grams using composition-based density values reported by Janney et al. [42]

Table 5
Average of nine analyses in Zone 3 of the high Pu/Zr/Mo phase and five analyses of the high U phase with 99% confidence interval errors.

	High Pu/Zr/Mo Phase	±	High U Phase	±
U wt%	71.0	0.71	85.3	1.02
Pu wt%	15.8	0.24	8.82	0.24
Am wt%	0.14	0.03	<0.05	
Zr wt%	9.15	0.14	0.24	0.06
Mo wt%	2.26	0.05	0.19	0.06
Ru wt%	0.63	0.03	<0.03	
Ce wt%	0.09	0.04	0.10	0.05
Cs wt%	0.04	0.01	0.07	0.03
Ba wt%	0.04	0.03	0.09	0.04
Total	99.15		94.81	

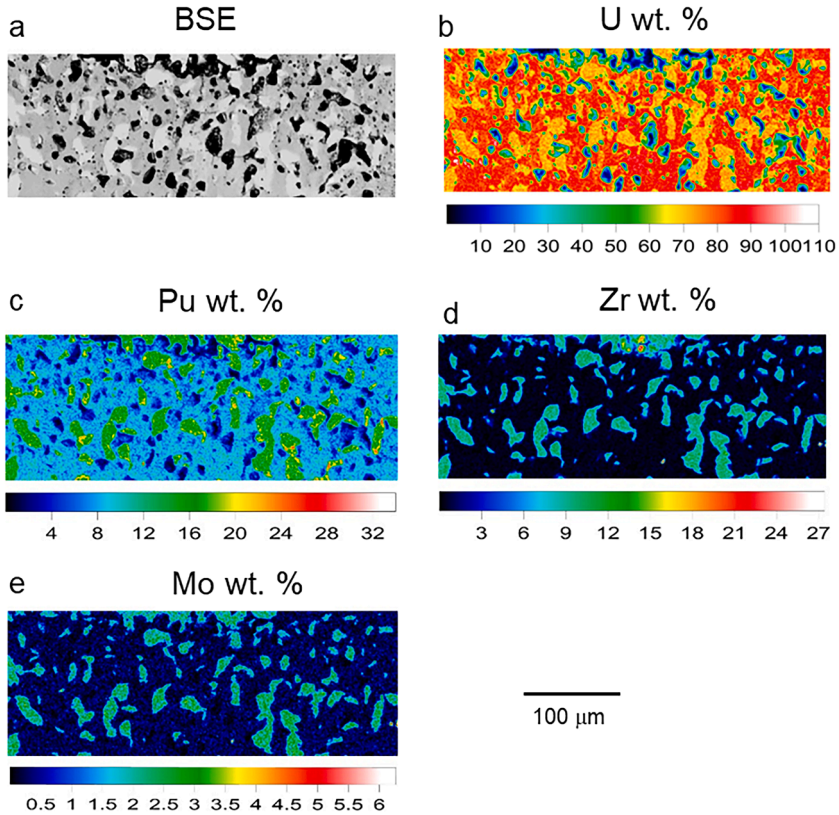

Fig. 6. (a–e). a) BSE micrograph of Zone 3 (Fig. 2, Box 3). (b–e) quantitative X-ray maps of U, Pu, Zr, and Mo, respectively.

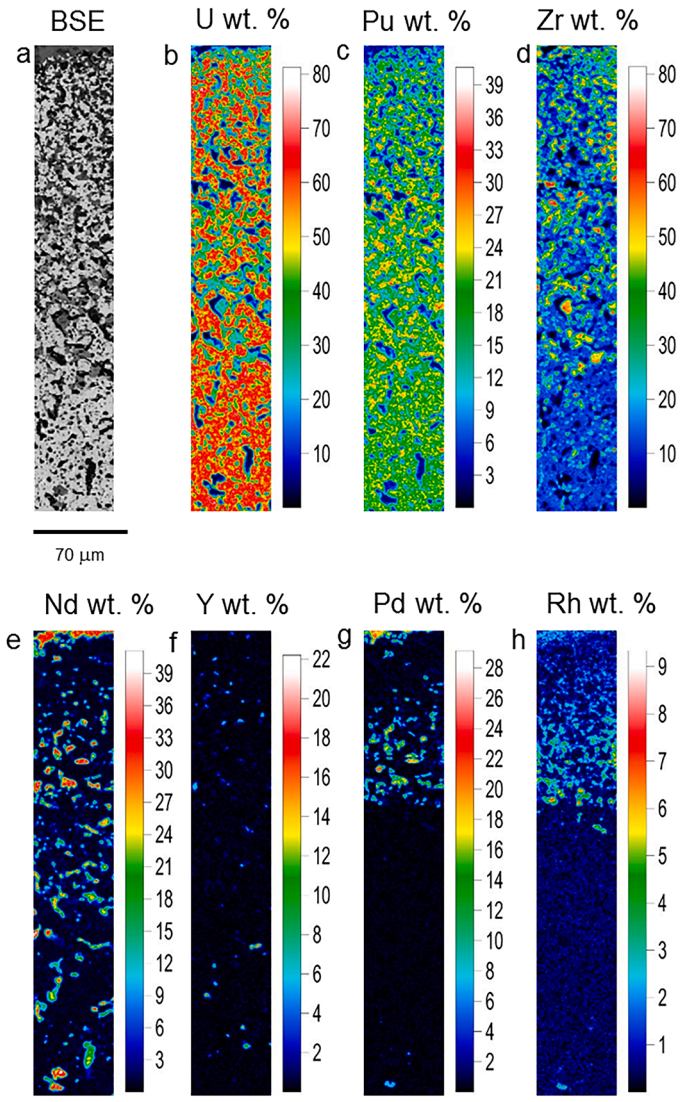

Fig. 7. (a–h). a) BSE micrographs of the outer portion of Zone 4 (Fig. 2, Box 4). (b–h) quantitative X-ray maps of U, Pu, Zr, Nd, Y, Pd, and Rh, respectively. The fuel-cladding interface is toward the top of each image.

and corrected for porosity based on porosity measurements reported in Table 3 of this work. The U, Pu, and Zr masses obtained from each semicircular slice are then added together to obtain the mass of each fuel chemical element within that half of the pin cross section (i.e. pin center to the "north" cladding interface). The process is then repeated for the second radial traverse (i.e. pin center to the "south" cladding interface) and the data are combined to represent the fuel element masses in each zone and within the entire examined fuel cross section. See [43] for more details about this technique.

Although it is possible to quantify fuel element mass gain and loss within each zone, the results do not discriminate between mass moving via advection or diffusion and mass changes resulting from nuclear processes such as activation, capture or fission (hereafter referred to as "nuclear processes" (NP)). Finally, to ascertain whether the EPMA-computed masses for the overall fuel element analysis cross section were reasonable, they were compared to those obtained using the bulk technique Q-ICP-MS to determine the EPMA method accuracy.

Table 6 shows the overall examined pin cross section fuel element concentrations (wt. %) for both Q-ICP-MS and EPMA, while Table 7 shows the overall percent gain/loss between the pre- and post-irradiation compositions as measured by both techniques. It is noteworthy how similar the results are. Not only is Q-ICP-MS a bulk

Table 6
Overall pin fuel element analysis for the as-fabricated pin, and the post-irradiated pin as measured by EPMA and Q-ICP-MS. Note that post-irradiation analytes sum to <100% because fission products are not included. Relative error values represent the 95% confidence interval.

	U	± relative %	Pu	± relative %	Zr	± relative %
Fabrication composition (wt %)	67		19		14	
Post-irradiation composition (QICPMS) (wt%)	63.0	5	16.3	5	14.5	5
Post-irradiation composition (EPMA) (wt %)	64.8	1.1	16.4	1.7	14.3	0.5/22*

*The larger error applies to Zr concentrations < 1 wt%.

Table 7
Shows the percentage loss/gain comparison between the as-fabricated composition and the post-irradiation composition as measured by Q-ICP-MS and EPMA.

	U	Pu	Zr
Q-ICP-MS	-5.95	-14.2	3.78
EPMA	-3.28	-13.7	2.14

measurement technique while EPMA is a spatially resolved technique, but their respective quantitative approaches are also quite different from one another. Thus, it is significant that the results from the two techniques compare quite favorably to one another (within ~3%, relative).

4.2. *Constituent redistribution*

Many efforts have been made to model component redistribution in the U-Pu-Zr metallic system. Having observed three distinct concentric compositional zones in the irradiated U-Pu-Zr ternary system, numerous workers [6,7,10,12–15,44] have forwarded the concept that this phenomenon can be explained via a radial temperature gradient that governs component solubility in phases and thus drives the phase assemblage in each compositional zone. One primary assumption these workers employ to simplify the modeling process is to assume that the Pu composition is either unchanging, or does not change significantly, thereby reducing the three-component system to a two-component system. This permits the use of a pseudo binary phase diagram [10,12,45] in which the Pu concentration is fixed at 19 wt.%, to explain the component redistribution process. Using this general approach combined with various modeling techniques, the U and Zr radial compositional profiles for some historical samples have been reproduced successfully [6,14,45].

Before phase diagrams are discussed in detail it is important to preface the discussion by clarifying that although the EPMA technique can measure elemental composition it is unable to determine crystallographic lattice parameters. Therefore, any phase identifications are tentative until crystallographic data can be obtained.

The use of phase diagrams and attendant phase properties to predict constituent redistribution in U-Pu-Zr fuel poses significant challenges. Firstly, one assumption inherent to the use of phase diagrams is that the system under consideration is at equilibrium. Phase diagrams illustrate what is thermodynamically possible but do not consider the effects of reaction kinetics or the impact of minor chemical contamination or elemental substitution on phase stability or equilibrium. Moreover, line and point crystal defects can be induced by radiation but are not well-quantified for materials exposed to fast neutrons. Some workers assert that assuming the irradiated U-Pu-Zr system is at equilibrium is a reasonable assumption [15,16]; however, it is not likely that all

processes are at equilibrium. Consider the observation that by 5 at. % burnup, the characteristic radially driven porosity patterns are well-developed in irradiated U-Pu-Zr fuel, but the constituent redistribution process remains ongoing [7].

Secondly, phase properties and fundamental fuel properties and behavior are not well understood. This includes phase dependent diffusion coefficients and heats of transport [15]. Moreover, although the use of pseudo binary diagrams simplifies the modeling process, inconsistencies have been noted between the use of reported enthalpies of solution and the simplified diagram [15].

To illustrate some of the complications introduced by using the pseudo binary phase diagram, data collected from this study has been plotted on the pseudo binary diagram of Ogata et al. [45] (Fig. 8a) and Kim et al. [12] (Fig. 8b) and ternary phase diagrams of O'Boyle and Dwight [46] in Fig. 9 (a, b). Unfortunately, no temperature profile data exist for this pin; zone temperatures are estimated based on chemical and evident phase changes and the known inner cladding temperature (Table 2).

Temperatures at which various compositional zones are plotted on the two pseudo binary diagrams were assigned based upon where those zones plotted on the ternary diagrams. Zone 3 comprises two distinct phases, a high U phase that plots in the βU phase field and a high Zr phase that plots in the γ1 + γ2 + βU phase field at 660 °C. Note that the γ phase is the bcc U phase with solubility for Pu (ε phase) and bcc Zr. The γ phase separates into two immiscible solids—γ1 (U-rich) and γ2 (Zr-rich). Since the weighted average of the two phases (Z3 $_{wa}$) plots on the line in the 660 °C ternary diagram where the γ phase separates, it is plausible that phase separation began at or around that temperature (Fig. 9a). A similar change appears to occur in Zone 2 at approximately 670 °C (Fig. 9b). In this case Zone 2 is situated on a phase line that separates

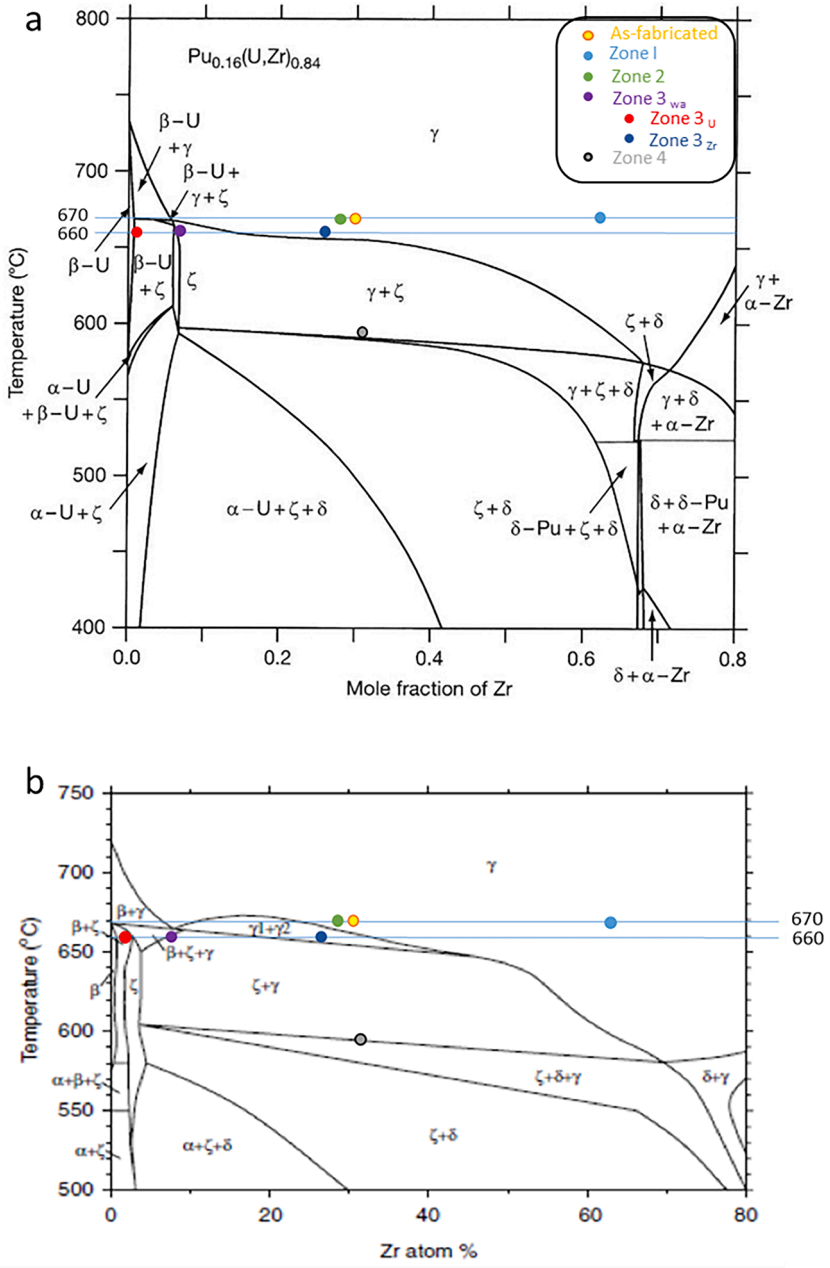

Fig. 8. (a, b). Shows the compositional zones described in Section 3 plotted on the pseudo binary U-Zr phase diagram of (a) Ogata et al. [45] and (b) Kim et al. [12]. Pu is fixed at 19 wt. % for both diagrams. The phase decomposition observed in Zone 3 is indicated by "Zone 3 $_{wa}$" (the weighted average of the two observed phases), "Zone 3 $_{Zr}$" (the high Zr-containing phase), and "Zone 3 $_{U}$" (the high U-containing phase). Other zones are indicated in the accompanying legend.

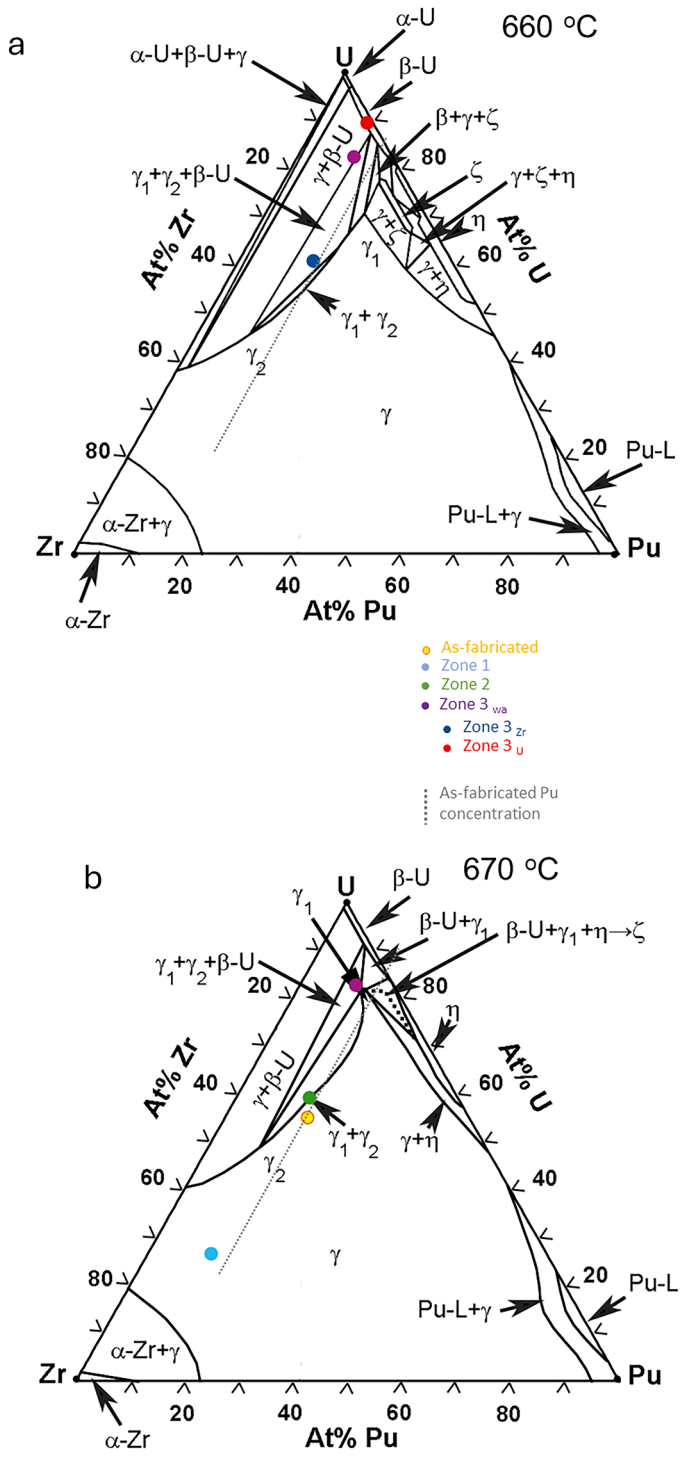

Fig. 9. (a, b). Shows compositional Zones 1-3 described in Section 3 plotted on ternary U-Pu-Zr phase diagrams of O'Boyle and Dwight [46] for temperatures: a) 660 °C (Zone 3); and b) 670 °C (Zones 1-3_{wa} and as-fabricated composition). The as-fabricated Pu composition line is shown by the gray dotted line. The phase decomposition observed in Zone 3 is indicated by "Zone 3_{wa}" (the weighted average of the two observed phases), "Zone 3_{Zr}" (the high Zr-containing phase), and "Zone 3_U" (the high U-containing phase). Other zones are indicated in the accompanying legend.

Zone 1 in the γ field from Zone 3_{wa} in the γ1+γ2+βU field at 670 °C. It is plausible that at approximately 670 °C, Zone 1 and Zone 2 became two distinct phases and that at 660 °C, Zones 2 and 3 became distinct phases. Since the inner cladding temperature was reported to be approximately 589°C (Table 2), Zone 4 is plotted on the 595°C ternary phase diagram, which places it in the γ + ζ zone for both the ternary diagram (data not shown) and the pseudo binary diagram of Ogata et al. [45] (Fig. 8a).

In comparing the phase(s) that correspond to each zone's composition, it can be seen that the corresponding phase field is not necessarily the same for the CALPHAD optimized pseudo binary diagrams and the empirically determined ternary diagrams (Table 8).

In comparing the Ogata et al. [45] pseudo binary diagram with the ternary diagrams [46], Specifically, both the pseudo binary diagram [45] and the ternary diagram assign the γ phase to Zone 1 and γ + ζ to Zone 4. However, differences occur in Zones 2 and 3. In Zone 2, the ternary diagram distinguishes between the $\gamma_1 + \gamma_2$ and γ phase fields while the pseudo binary diagram [45] uses the γ phase designation only. The pseudo binary diagram [45] assigns the γ + ζ designation to Zone 3_{wa}, but the ternary diagram assigns γ + βU to that zone. Finally, Zone 3_{Zr} is assigned to the γ phase field in the pseudo binary diagram, whereas the ternary diagram designates that phase field as $\gamma_1 + \gamma_2 + \beta U$.

Although the pseudo binary diagrams of Ogata et al. [45] and Kim et al. [12] both fix Pu at 19 wt%, the phase field assignments differ somewhat between the two diagrams. Zones 1, 2, 3_{wa} and 3 U are assigned the same field for both authors' pseudo binary diagrams—γ, γ, γ + ζ, and ζ + βU, respectively. However, phase field assignments for Zone 3_{Zr} and Zone 4 differ between the two authors. In general, the two pseudo binary diagrams assign a ζ component to phase fields (e.g. Zone 3_{wa}, Zone 3_U) whereas βU is a more common component in the ternary diagrams [46].

This suggests that not only do the U-Zr pseudo binary diagrams not predict the same phase field assignments as the ternary U-Pu-Zr phase diagrams predict, but that pseudo binary U-Zr diagrams calculated by different workers do not necessarily agree with each other.

The second complication with using phase diagrams as the basis for model construction lies with the practice of fixing the Pu content at 19 wt.% (~15 at. %). If the Pu concentration had remained constant at approximately 15 at. % during irradiation (this work), the presumed phase identifications for the compositional zones on the ternary diagrams would correspond to those in Table 9 (fixed Pu). For plotting purposes, it is assumed that the number of moles added or subtracted to

Table 8
Compares the phase field corresponding to each identified zone's U-Zr composition (pseudo binary diagrams) and U-Pu-Zr composition (ternary diagram). The pseudo binary diagrams comes from Ogata et al. [45] and Kim et al. [12] while the ternary diagrams come from O'Boyle and Dwight [46].

Diagram	Zone 1	Zone 2	Zone 3_{wa}	Zone 3_{Zr}	Zone 3_U	Zone 4
Pseudo Binary Diagram [45] (670 °C)	γ	γ				
Pseudo Binary Diagram [12] (670 °C)	γ	γ				
Ternary Diagram [46] (670 °C)	γ	γ1 + γ2	γ1 + γ2 + βU			
Pseudo Binary Diagram [45] (660 °C)			γ + ζ	γ	ζ + βU	
Pseudo Binary Diagram [12] (660 °C)			γ + ζ	γ1 + γ2	ζ + βU	
Ternary Diagram [46] (660 °C)			γ + βU	γ1 + γ2 + βU	βU	
Pseudo Binary Diagram [45] (595 °C)						γ + ζ
Pseudo Binary Diagram [12] (595 °C)						γ + ζ + δ
Ternary Diagram [46] (595 °C)						γ + ζ

Table 9
Compares the phase field corresponding to each identified zone's composition as plotted on U-Pu-Zr ternary diagrams with measured Pu and Pu fixed at the fabrication concentration. Differences are highlighted in red. The ternary diagrams come from O'Boyle and Dwight [46].

	Ternary diagram (measured Pu)	Ternary diagram (fixed Pu)
Zone 1	γ	γ
Zone 2	$\gamma_1 + \gamma_2$ (670 °C)	γ (670 °C)
Zone 3_{wa}	βU + γ (660 °C)	βU + γ_1 (660 °C)
Zone 3_{Zr}	$\gamma_1 + \gamma_2$ + βU (660 °C)	$\gamma_1 + \gamma_2$ (660 °C)
Zone 3_U	βU (660 °C)	* (660 °C)
Zone 4	γ + ζ (595 °C)	γ + ζ (595 °C)

* does not plot on the diagram

achieve a constant Pu concentration of 15.4 at% is compensated by dividing that number of moles in half and adding/subtracting those values to U and Zr at. % concentrations. When these changes are made, the $\gamma_1 + \gamma_2$ phases present in the quantitatively measured Pu plot change to γ in the fixed Pu plot. Similarly, the γ phase in Zone 3_{wa} changes to γ_1 in the fixed Pu plot. Zone 3_{Zr} loses the βU component in the fixed Pu plot while Zone 3_U cannot be plotted on the fixed Pu diagram. This is because subtracting the necessary quantity of Zr to increase Pu leads to a negative Zr concentration. When Pu is fixed at the fabrication concentration, the phase fields associated with each zone's compositions gravitate to those with greater Pu enrichment, which does not accurately represent the compositions measured during this work and subsequently presented here.

4.3. EPMA-calculated mass changes by zone

Section 4.1 and Table 6 demonstrated that although EPMA- and Q-ICP-MS-measured overall fuel cross section elemental composition for the irradiated U-19Pu-14Zr sample was determined with vastly different techniques, the results were within 3% (relative) of each other. This suggests that although it is difficult to quantify the total error for the EPMA-based technique, its error is no larger than the error for Q-ICP-MS, which can be determined much more easily. This is an important point because the data obtained by employing the technique described in Section 4.1 can be used to determine fuel element masses and attendant mole quantities to quantify atom content changes in each compositional zone.

In this section, U, Pu, and Zr masses for each zone as calculated by EPMA for Section 4.1 were converted to nanomoles to quantify atom gain or loss between compositional zones. Table 10 shows the pre-irradiated U, Pu, and Zr atom content while Table 11 shows the post-irradiation atom content. Table 12 shows the atom content change for each component in each zone.

Table 12 shows that the number of U atoms lost from Zone 1 (0.8 nmoles) is about 10% lower than the number of U atoms gained by Zones 2 and 3 (0.88 nmoles), suggesting the possibility that U loss from Zone 1 accumulates in Zones 2 and 3. Pu atoms are lost from all four zones, though the largest percentage loss occurs with Zones 1 and 3 (-39.8% and -21.9%, respectively). Zr atom loss from Zone 3 (0.45 nmoles) is nearly equal to the quantity gained by Zones 1 and 2 (0.48 nmoles). Because Zr is produced from fission, an increase in the number of Zr atoms is expected. Zone 4 was not observed to lose Zr atoms.

Table 10
Shows the pre-irradiation fuel element zone content in nmoles. This calculation encompasses the entire fuel cross section area to a depth of 1 μm.

	U nmole	Pu nmole	Zr nmole
Zone 1	1.30	0.36	0.70
Zone 2	0.46	0.13	0.25
Zone 3_{wa}	1.10	0.31	0.59
Zone 4	3.51	0.98	1.89
Total	6.37	1.78	3.43

Table 11
Shows the post-irradiation fuel element zone content in nmoles. This calculation encompasses the entire fuel cross section area to a depth of 1 μm.

	U nmole	Pu nmole	Zr nmole
Zone 1	0.50	0.22	1.17
Zone 2	0.55	0.12	0.26
Zone 3_{wa}	1.89	0.24	0.14
Zone 4	3.11	0.93	1.89

Table 12
Shows the fuel element content change (in nmoles) following irradiation.

	U nmole	Pu nmole	Zr nmole
Zone 1	-0.80	-0.14	0.47
Zone 2	0.09	-0.01	0.01
Zone 3_{wa}	0.79	-0.07	-0.45
Zone 4	-0.40	-0.05	0.00
gain/loss	-0.32	-0.27	0.03
gain/loss (%)	-5.02	-15.2	0.87

What is not discernable with this work is the interplay between NP and mass transport. For example, although U, Pu, and Zr exhibit quantifiable radial concentration changes, with the assembled data in this work it is not possible to determine how NP influenced the radial concentration profiles versus how mass transport processes alter radial concentration profiles. However, it is known that in a true fast reactor spectrum the radial power density is uniform because the neutron mean free path is much larger than the pin diameter. Therefore, the initial fission density in each zone should be similar.

The data assembled here provides a modern modeling framework that can be used to assist modelers in developing more accurate constituent redistribution models for irradiated U-Pu-Zr metallic fuel.

4.4. Plutonium redistribution

Numerous references [6,9,10,12–15] describe the post-irradiation Pu radial concentration profile in irradiated U-Pu-Zr fuels as unchanging, or without significant changes. This conclusion appears to result from early EPMA data obtained from U-19Pu-10Zr Pin T-179, which experienced a 1.9 at. % burnup. It is not clear whether the EPMA Pu measurements were flawed due to the use of measurement practices described in Section 1.2, or whether Pu migration had not yet occurred due to the low burnup, although [17] suggests the latter.

Ref. [21] describes EPMA analysis of U-19Pu-10Zr pin DP-16, which experienced a ~10 at. % burnup. This higher burnup sample is similar to the sample examined in this work, which makes it a better comparison than T-179.

This Ref. [21] shows the elemental analysis of seven different points spanning the DP-16 fuel radius, in which Pu concentrations vary from 4 wt. % (in a fission-product phase) to 19 wt. % near the cladding. The problem with these analyses is that they have not been analyzed for a substantial quantity of the elemental mass, which means that these analyses are not accurate. Accurate microanalysis (EPMA or scanning electron microscopy) requires that a substantial quantity of the elemental mass be analyzed so that matrix corrections (atomic number, absorption, fluorescence) can be employed correctly. In this analysis, elemental analytical totals ranged from 10 wt. % (in the fission-product phase) to 96 wt. % in the high-U region, with most totals ranging from 70-88 wt. %); thus, the analyses show Pu variability, but it is not a quantitative analysis. Qualitative radial intensity profiles in DP-16 [21] show that Pu intensity is generally unchanged from the center to the cladding, except for a slight decrease in the mid-radius location. However, because of the EPMA measurement practices that occurred historically (Section 1.2), it is not possible to determine whether this slight decrease represents a measurable concentration change or not.

Ref. [22] shows a modern EPMA analysis of a U-19Pu-10Zr METAPHIX fuel irradiated to a burnup of 7.0 at. %. While the elemental redistribution pattern in this sample is quite different from that shown in this study, the Pu radial concentration ranges from ~8 to ~22 wt. %, which is comparable to that observed in the present study. If we consider the atomic content data presented in Tables 10–12 of this study, the post-irradiation Pu atomic content of each zone is lower than the as-fabricated content as measured both by moles of Pu and the percentage of Pu lost due to NP or transport. This suggests that the assumption of Pu as a spatially invariant quantity or atomic fraction is incorrect and therefore warrants incorporation into constituent redistribution models.

4.5. Suggestions for future work

Firstly, although the EPMA-collected data and attendant calculations for U, Pu, and Zr atom loss/gain provide insight into mass changes occurring during irradiation, it is necessary to distinguish between mass changes resulting from transport processes versus mass changes due to NP. Determining the radial burnup profile (if possible) or determining the radial U-235/Pu-239 isotopic profile via laser ablation or secondary ion mass spectroscopy will help to separate the two phenomena.

For example, although the number of U atoms lost from Zone 1 is approximately equal to the number of U atoms gained in Zones 2 and 3, it is not likely that U lost from Zone 4 is due entirely to nuclear processes. It is more likely that each zone has experienced a combination of elemental radial fuel element transport and NP.

Secondly, fission products should be similarly quantified by zone location. This effort can provide insight into the question of what proportion of mass changes are due to diffusion or advection versus NP.

Finally, this data suggests modeling efforts might be improved if workers: 1) experiment with allowing Pu concentrations to vary as this data shows that it does; 2) consider the possibility that the system is continuing to evolve chemically as evidenced by the large compositional changes occurring across narrow Zone 2; 3) use modern EPMA-generated data sets to verify model predictions; and 4) use micro X-ray diffraction (mXRD) techniques to determine the phase assemblage in each zone, thereby ascertaining the degree to which equilibrium phase diagrams represent actual irradiated systems. Although transmission electron microscopy can be used to measure lattice parameters, the longer length scales afforded by mXRD are more comparable to the length scales represented by EPMA compositional measurements.

5. Conclusions

EPMA-based spatially resolved quantification of U, Pu, and Zr in irradiated U-19Pu-14Zr compares favorably to bulk chemical data obtained from ICP-based methods.

EPMA mass balance methods can quantify changes in the number of atoms of U, Pu, and Zr among the four compositional zones that characterize this sample, although it cannot distinguish between changes resulting from diffusion or advection from those resulting from nuclear processes.

This work demonstrates conclusively that the Pu radial concentration does not remain constant across the radius as assumed previously. Changes are significant enough to alter the presumed phase identity in ternary diagrams, such that Pu should be incorporated into constituent redistribution models, and pseudo binary diagrams should be avoided.

CRediT authorship contribution statement

Karen E. Wright: Writing – original draft, Methodology, Investigation, Data curation, Conceptualization. **Lindsey Lecrivain:** Writing – original draft, Investigation. **Cortney Pincock:** Investigation. **Magen Coleman:** Investigation. **Pamela Wiscaver:** Investigation. **Beau Barker:** Validation. **Luiza Gimenes Rodrigues Albuquerque:** Validation. **Luca Capriotti:** Writing – review & editing, Project administration. **Assel Aitkaliyeva:** Writing – review & editing, Funding acquisition.

Declaration of competing interest

The authors declare the following financial interests/personal relationships which may be considered as potential competing interests:

Assel Aitkaliyeva reports financial support was provided by US Department of Energy. If there are other authors, they declare that they have no known competing financial interests or personal relationships that could have appeared to influence the work reported in this paper.

Data availability

Data will be made available on request.

Acknowledgements

We thank the National Scientific Users Facility (NSUF) for their financial support. This work was sponsored by the U.S. Department of Energy, Office of Nuclear Energy, under U.S. Department of Energy Idaho Operations Office Contract DE-AC07-05ID14517. We are grateful for the thorough review and comments of two anonymous reviewers. The United States Government retains and the publisher, by accepting the article for publication, acknowledges that the United States Government retains a nonexclusive, paid-up, irrevocable, world-wide license to publish or reproduce the published form of this manuscript, or allow others to do so, for United States Government purposes.

References

[1] G. Locatelli, M. Mancini, N. Todeschini, Generation IV nuclear reactors: current status and future prospects, Energy Policy 61 (2013) 1503–1520, https://doi.org/10.1016/j.enpol.2013.03.101.
[2] W.J. Carmack, D.L. Porter, Y.I. Chang, S.L. Hayes, M.K. Meyer, D.E. Burkes, C. B. Lee, T. Mizuno, F. Delage, J. Somers, Metallic fuels for advanced reactors, J. Nucl. Mater. 392 (2009) 139–150, https://doi.org/10.1016/j.jnucmat.2009.03.007.
[3] D.C. Crawford, D.L. Porter, S.L. Hayes, Fuels for sodium-cooled fast reactors: US perspective, J. Nucl. Mater. 371 (2007) 202–231, https://doi.org/10.1016/j.jnucmat.2007.05.010.
[4] H.E. Garcia, M.J. Lineberry, S.E. Aumeier, H.F. McFarlane, Proliferation resistance of advanced sustainable nuclear fuel cycles, in: Proceedings of the Global 2001 International Conference On: "Back-End of the Fuel Cycle: From Research to Solutions, Paris 2001, 2001, 9-13 Sep.
[5] W.F. Murphy, W.N. Beck, F.L. Brown, B.J. Kaprowski, L.A. Neimark, (1969), ANL-7602, Argonne National Laboratory, Idaho Falls, ID.
[6] Y.S. Kim, G.L. Hofman, S.L. Hayes, Y.H. Sohn, Constituent redistribution in U-Pu-Zr fuel during irradiation, J. Nucl. Mater. 327 (2004) 27–36, https://doi.org/10.1016/j.jnucmat.2004.01.012.
[7] D.L. Porter, C.E. Lahm, R.G. Pahl, Fuel constituent redistribution during the early stages of U-Pu-Zr irradiation, Metall. Trans. A 21A (1990) 1871–1876.
[8] M.C. Petri, M.A. Dayananda, Isothermal diffusion in uranium-plutonium-zirconium alloys, J. Nucl. Mater. 240 (1997) 131–143.
[9] Y.H. Sohn, M.A. Dayananda, G.L. Hofman, R.V. Strain, S.L. Hayes, Analysis of constituent redistribution in the γ (bcc) U-Pu-Zr alloys under gradients of temperature and concentrations, J. Nucl. Mater. 279 (2000) 317–329.
[10] M. Ishida, T. Ogata, M. Kinoshita, Constituent migration model for U-Pu-Zr metallic fast reactor fuel, Nucl. Technol. 104 (1) (1993) 37–51, https://doi.org/10.13182/NT93-A34868.
[11] G.L. Hofman, S.L. Hayes, M.C. Petri, Temperature gradient driven constituent redistribution in U-Zr alloys, J. Nucl. Mater. 227 (1996) 277–286.
[12] Y.S. Kim, S.L. Hayes, G.L. Hofman, A.M. Yacout, Modeling of constituent redistribution in U-Pu-Zr metallic fuel, J. Nucl. Mater. 359 (2006) 17–28.
[13] A. Karahan (2009), Modeling of thermo-mechanical and irradiation behavior of metallic and oxide fuels for sodium fast reactors, Doctoral Dissertation, Massachusetts Institute of Technology.
[14] J. Galloway, C. Unal, N. Carlson, D. Porter, S. Hayes, Modeling constituent redistribution in U-Pu-Zr metallic fuel using the advanced fuel performance code BISON, Nucl. Eng. Des. 286 (2015) 1–17, https://doi.org/10.1016/j.nucengdes.2015.01.014.
[15] J. Hirschhorn, M. Tonks, C. Matthews, A CALPHAD-informed approach to modeling constituent redistribution in Zr-based metallic fuels using BISON, J. Nucl. Mater. (2021), https://doi.org/10.1016/j.jnucmat.2020.152657.

[16] M. Poschmann, M.H.A. Piro, T.M. Besmann, K.T. Clarno, S. Simunovic, Thermochemically-informed mass transport model for interdiffusion of U and Zr in irradiated U-Pu-Zr fuel with fission products, J. Nucl. Mater. (2021), https://doi.org/10.1016/j.jnucmat.2021.153089.
[17] Monte CArlo simulation of electroN trajectory in sOlids (Casino) v. 2.5.1.0, Universite de Sherbrooke, Sherbrooke, Canada, 2017.
[18] J.E. Sanecki (1986), Results of electron microprobe examination of specimen from IFR Rod T-042 (A/G 333C14), Argonne National Laboratory intra-laboratory memo, December 11, 1986.
[19] J.E. Sanecki (1987), Results of Electron Microprobe Examination of Specimen from IFR Element T459 (A/G 341B11), Argonne National Laboratory intra-laboratory memo, July 8, 1987.
[20] J.E. Sanecki (1991), Results of electron microprobe examination of two specimens taken from IFR fuel element DP-81, Argonne National Laboratory intra-laboratory memo, October 1, 1991.
[21] A.B. Cohen, J. E. Sanecki (1992), Results of electron microprobe examination of as-irradiated DP-16 (U-19Pu-10Zr/HT9) specimen, Argonne National Laboratory intra-laboratory memo, April 2, 1992.
[22] S. Bremier, K. Inagaki, L. Capriotti, P. Poeml, T. Ogata, H. Ohta, V.V. Rondinella, Electron probe microanalysis of a METAPHIX UPuZr metallic alloy fuel irradiated to 7.0 at.% burn-up, J. Nucl. Mater. (2016), https://doi.org/10.1016/j.jnucmat.2016.07.060.
[23] S. Bremier, P. Poeml, L. Capriotti, J. Himbert, V.V. Rondinella, H. Ohta, T. Ogata, Electron microprobe examination of irradiated metallic fuel containing rare earth and minor actinide elements, Trans. Am. Nucl. Soc. 117 (2017) 2017. VOct 29- Nov 2.
[24] C.W. Wilkes, G.L. Batte, D.B. Tracy, V. Griffiths, EBR-II Fuel Slug Casting Experience, Argonne National Laboratory, 1987. Report ANL-IFR-73.
[25] L. Capriotti, K.E. Wright, F.G. DiLemma, T.L. Trowbridge, A. Aitkaliyeva, T. Rahn (2022), Engineering & microstructure scale PIE report on EBR-II X441A metallic fuel pins for the MORPH experiment, 10.2172/2283741.
[26] K.E. Wright, J.M. Harp, L. Capriotti, Electron probe microanalysis of irradiated FUTURIX-FTA U-Pu-Zr alloy with added minor actinides, J. Nucl. Mater. (2019), https://doi.org/10.1016/j.jnucmat.2019.151745.
[27] X. Ritter, P. Poeml, H. Ohta, S. Bremier, J. Himbert, R. Hasnaoui, J. Berndt, Improved protocol for the quantification of actinides (Th, U, Np, Pu, Am, and Cm) using electron probe microanalysis, Microsc. Microanal. 27 (2021) 1056–1068, https://doi.org/10.1017//S1431927621012526.
[28] J. Donovan (2023), Probe for EPMA v. 13.3.1, Probe Software, https://www.probesoftware.com/.
[29] Cameca (2017), Peak Sight v. 5.1, https://www.cameca.com/service/software/peaksight.
[30] J. Donovan (2023), Probe image v. 1.3.5.2115, probe software, https://www.probesoftware.com/.
[31] K.F.J. Heinrich (1987), Mass absorption coefficients for electron probe microanalysis, in Proc. ICXOM XI, J.D. Brown and R.H. Packwood, eds, p. 67-119, London, Ontario: University of Western Ontario Press.
[32] J.L. Pouchou, F. Pichoir, Quantitative analysis of homogeneous or stratified microvolumes applying the model, "PAP", in K.F.J. Heinrich and D. E. Newbury (eds.). Electron Probe Quantification, Plenum Press, New York, 1991, pp. 31–76.
[33] I.R. Farthing, C.T. Walker, (1990), Heinrich's Mass Absorption Coefficients for the K, L, and M Lines, The European Commission, Institute for Transuranium Elements, Karlsruhe, Report K0290140.
[34] https://highpuritystandards.com/products/categories/icp-ms-single-and-multi-component-standards/, 2024.
[35] https://www.energy.gov/nnsa/articles/nbl-program-office-certificate-analysis-certified-reference-material-c129a-1guranium, 2024.
[36] https://www.energy.gov/nnsa/articles/nbl-program-office-certificate-analysis-certified-reference-material-c126-0, 2024.
[37] Metrodata GmbH: GUM Workbench© Pro Version - English, Version 2.4.1.406 (http://www.metrodata.de/ver24_en.html), 2024.
[38] D.E. Burkes, R.S. Fielding, D.L. Porter, D.C Crawford, M.K. Meyer, A US perspective on fast fuel fabrication technology and experience part I: metal fuels and assembly design, J. Nucl. Mater. 389 (2009) 458–469, https://doi.org/10.1016/jnuclmat.2009.02.035.
[39] ImageJ v. 1.51k, National Institutes of Health, USA, http://imagej.nih.gov/ij, 2024.
[40] T. Rahn, L. Capriotti, F. DiLemma, T.L. Trowbridge, J.M. Harp, A. Aitkaliyeva, Investigation of constituent redistribution in U-Pu-Zr fuels and its dependence on varying Zr content, J. Nucl. Mater. 557 (2021) 153301, https://doi.org/10.1016/j.jnucmat.2021.153301.
[41] H. Okamoto, Nd-Pd phase diagram, J. Phase Equilibria 13 (1992) 220–222.
[42] D. Janney, C. Papesch (2017) Metallic Fuels Handbook, Part 1: alloys based on U-Zr, Pu-Zr, U-Pu, or U-Pu-Zr including those with minor actinides (np, Am, Cm), rare-earth elements (La, Ce, Pr, Nd, Gd), and Y; and Part 2: elements and alloys not based on U-Zr, Pu-Zr, U-Pu, or U-Pu-Zr, 10.2172/1504934.
[43] K.E. Wright, J. Stempien, W. Jiang, I.J. van Rooyen, Fission product distribution in irradiated safety-tested and as-irradiated AGR-2 TRISO particles, J. Nucl. Mater. (2022) 153468, https://doi.org/10.1016/j.jnucmat.2021.153468.
[44] J. Hirschhorn, M. Tonks, A. Aitkaliyeva, C. Adkins, Development and verification of a phase-field model for the equilibrium thermodynamics of U-Pu-Zr, Ann. Nucl. Energy (2019), https://doi.org/10.1016/j.anucene.2018.10.029.
[45] T. Ogata, Y.S. Kim, A.M. Yacout, Metal fuel performance modeling and simulation, in eds. R.J.M. Konings, T.R. Allen, R.E. Stoller, S. Yamanaka, in: Comprehensive Nuclear Materials, 3, Elsevier Publishing, The Netherlands, 2012, pp. 1–40. v.
[46] D.R. O'Boyle, A.E. Dwight, The uranium-plutonium-zirconium ternary alloy system, in: W.N. Miner (Ed.). Plutonium 1970 and Other Actinides, Metallurgical Society of AIME, 1970, pp. 720–732.